Cross-Linked CoMoO$_4$/rGO Nanosheets as Oxygen Reduction Catalyst

Jiaqi Fu [1], Jiang-Li Meng [1], Mei-Jie Wei [1], Hong-Ying Zang [1],*, Hua-Qiao Tan [1], Yong-Hui Wang [1],*, Haralampos N. Miras [2],* [ID] and Yang-Guang Li [1],*

[1] Key Laboratory of Polyoxometalate Science of Ministry of Education, Key Laboratory of Nanobiosensing and Nanobioanalysis at Universities of Jilin Province, Faculty of Chemistry, Northeast Normal University, Changchun 130024, China; fujq140@nenu.edu.cn (J.F.); mengjl480@nenu.edu.cn (J.-L.M.); weimj212@nenu.edu.cn (M.-J.W.); tanhq870@nenu.edu.cn (H.-Q.T.)
[2] School of Chemistry, The University of Glasgow, Galsgow G12 8QQ, UK
* Correspondence: zanghy100@nenu.edu.cn (H.-Y.Z.); wangyh319@nenu.edu.cn (Y.-H.W.); harism@chem.gla.ac.uk (H.N.M.); liyg658@nenu.edu.cn (Y.-G.L.); Tel.: +86-431-8568-4009 (H.-Y.Z. & Y.-H.W. & Y.-G.L.)

Abstract: Development of inexpensive and robust electrocatalysts towards oxygen reduction reaction (ORR) is crucial for the cost-affordable manufacturing of metal-air batteries and fuel cells. Here we show that cross-linked CoMoO$_4$ nanosheets and reduced graphene oxide (CoMoO$_4$/rGO) can be integrated in a hybrid material under one-pot hydrothermal conditions, yielding a composite material with promising catalytic activity for oxygen reduction reaction (ORR). Cyclic voltammetry (CV) and linear sweep voltammetry (LSV) were used to investigate the efficiency of the fabricated CoMoO$_4$/rGO catalyst towards ORR in alkaline conditions. The CoMoO$_4$/rGO composite revealed the main reduction peak and onset potential centered at 0.78 and 0.89 V (vs. RHE), respectively. This study shows that the CoMoO$_4$/rGO composite is a highly promising catalyst for the ORR under alkaline conditions, and potential noble metal replacement cathode in fuel cells and metal-air batteries.

Keywords: CoMoO$_4$ nanosheets; reduced graphene oxide; hydrothermal reaction; oxygen reduction reaction; fuel cell

1. Introduction

The exponential increase of energy demand and serious environmental problems induce the growth of clean and sustainable energy [1–5]. The electrochemical oxygen reduction reaction (ORR) and oxygen evolution reaction (OER) have been deemed as two main processes which are highly important in green energy applications. From these two processes, the ORR is the determinant reaction in fuel cells and metal-air batteries [6–9].

ORR is inherently complicated and has sluggish oxygen reduction kinetics in both fuel cells and metal-air batteries [10]. At present, Pt and Pt based alloys catalysts have been conceded as the best ORR catalysts [11,12]; however platinum's scarcity in the earth's crust, its high cost, and poor stability have prevented widespread commercial application. In an effort to overcome the above issues, extensive research efforts have been focused on the devise and synthesis of ORR electrocatalysts based on transition-metal elements which are cheap, highly active, and stable over the long term.

Transition metal elements such as iron, manganese, nickel, and cobalt were investigated as potential low-cost and earth-abundant catalysts towards ORR under alkaline condition [13–18]. Binary metal oxides and mixed metal oxides have been considered due to their good performance for ORR, such as ZnCo$_2$O$_4$ [19], Zn$_2$SnO$_4$ [20], NiCo$_2$O$_4$ [21], NiMoO$_4$ [22], and CoMoO$_4$ [23,24]. Additionally, transition metal oxides have attracted the attention of research groups and have been widely utilized as

bifunctional catalysts due to their multiple oxidation states, which is apt to be used in electrocatalytic processes. The relevant materials that can adopt different oxidation states which are directly related to the observed functionality and activity in various processes while they can contribute to the stability of an electrolytic cell. Also, in marked contrast to the noble metal catalysts, transition metal oxides are earth-abundant and cheaper [25]. Lately metal molybdates were proposed to be an outstanding candidate in electrochemical energy conversion, such as water-splitting and lithium-ion batteries, indicative of their rapid and efficient redox activity. Metal molybdates illustrate exceptional stability in alkaline solution. Especially $CoMoO_4$ is deemed as a highly promising ORR catalyst due to its low cost, low toxicity, abundance, and durability. Yet, $CoMoO_4$ nanostructure also exhibits the disadvantage of easy aggregation. So, there have only been rare reports on the synthesis of highly dispersed $CoMoO_4$ nanostructure with good electrocatalytic activity via hydrothermal synthesis. A general means to tackle this issue is to devise and synthesize an appropriate material exhibiting high conductivity, evenly distributed catalytic active sites, increase the onset potential which will finally boost the reaction rates [26].

It has been reported that carbon based components like graphene and single-walled carbon nanotubes (SWNTs) have been routinely used for the preparation of hybrid materials as ORR electrocatalysts, in supercapacitors and proton-exchange-membrane fuel cells, owing to their extraordinary performances arising from their big surface area, high conductivity, and structural flexibility [27–30]. Graphene intrinsically has numerous advantages such as high specific surface area which can easily contact with electrolyte solution and long term electrochemical stability, making it a superb substrate for high-property electrocatalysis reactions.

Herein, we report the preparation and characterization of a hybrid material composed of $CoMoO_4$ nanosheets and reduced graphene oxide as well as its efficiency as ORR catalyst in alkaline media. $CoMoO_4$ nanosheets grown on rGO revealed improved conductivity, increased active area and enhanced contact of the electrolyte solution with the electrode material. Cooperative effects of the composite's components revealed improved ORR performance and higher stability compared to pristine $CoMoO_4$ or rGO.

2. Results and Discussion

X-ray Powder Diffraction (XRD) patterns for the as-prepared materials were presented in Figure 1a. The main diffraction peaks at 2θ of 27.5°, 33.7°, 58.4° in both $CoMoO_4$/rGO and $CoMoO_4$ are attributed to the (−2 0 2), (−2 2 2), (0 2 4) lattice planes, respectively, which is consistent with the $CoMoO_4$ (JCPDS, card No. 21-0868). The weak and wide diffraction peak at 2θ of 26.1° in rGO is corresponding to the lattice plane of (0 0 2). The result implies the formation of a carbon framework with relatively higher degree of graphitization. The (0 0 2) diffraction peak becomes lightly weaker and wider in $CoMoO_4$/rGO, this means that the degree of crystallization of the rGO decreases due to the incorporation of $CoMoO_4$.

The degree of defect in carbon materials can be studied by Raman spectroscopy. We observed the Raman spectrum of $CoMoO_4$/rGO. As shown in Figure 1b, we can clearly observe that there are mainly seven peaks in the $CoMoO_4$/rGO sample, centered at 339, 670, 817, 879, 932 cm^{-1}, corresponding to the Co–Mo–O bond stretching vibration. D-band and G-band peaks of rGO were centered at 1361 and 1600 cm^{-1}, respectively. The G band expresses sp^2 carbon atoms possession, the D is usually connected with the vibration of sp^3 carbon atoms [31]. Furthermore, the intensity ratio of the D peak and the G peak exhibits a structural defect density on the surface of the carbon nanomaterial [32]. The Raman spectra of $CoMoO_4$/rGO shows that the I_D/I_G ratio (1.09) is higher than the ratio observed in pristine graphene oxide (0.87; Figure S1), indicating that the $CoMoO_4$/rGO composite exhibits more structural defects which can be beneficial for the ORR.

The morphology of the prepared composite was studied by SEM (Figure 1c,d) and TEM (Figure 1e,f). As shown in Figure 1c,d, the cross-linked $CoMoO_4$ nanosheets were assembled on rGO by a conventional hydrothermal process. From the scanning electron microscope (SEM) images of

$CoMoO_4$/rGO, it was obviously demonstrated that $CoMoO_4$ nanosheets were well embedded into the graphene nanosheets, but a part of the $CoMoO_4$ nanosheets was easier to agglomerate on the surface of graphene. Thus the doped graphene can further hinder the aggregation of $CoMoO_4$ so that it can increase the accessibility of multiple active sites with direct consequences to the performance of the composite material.

From the transmission electron microscope (TEM) pictures (Figure 1e,f), it can be evidently seen that $CoMoO_4$ is deposited (darker areas in the TEM image) on the surface of rGO, indicating that $CoMoO_4$/rGO composite has been synthesized.
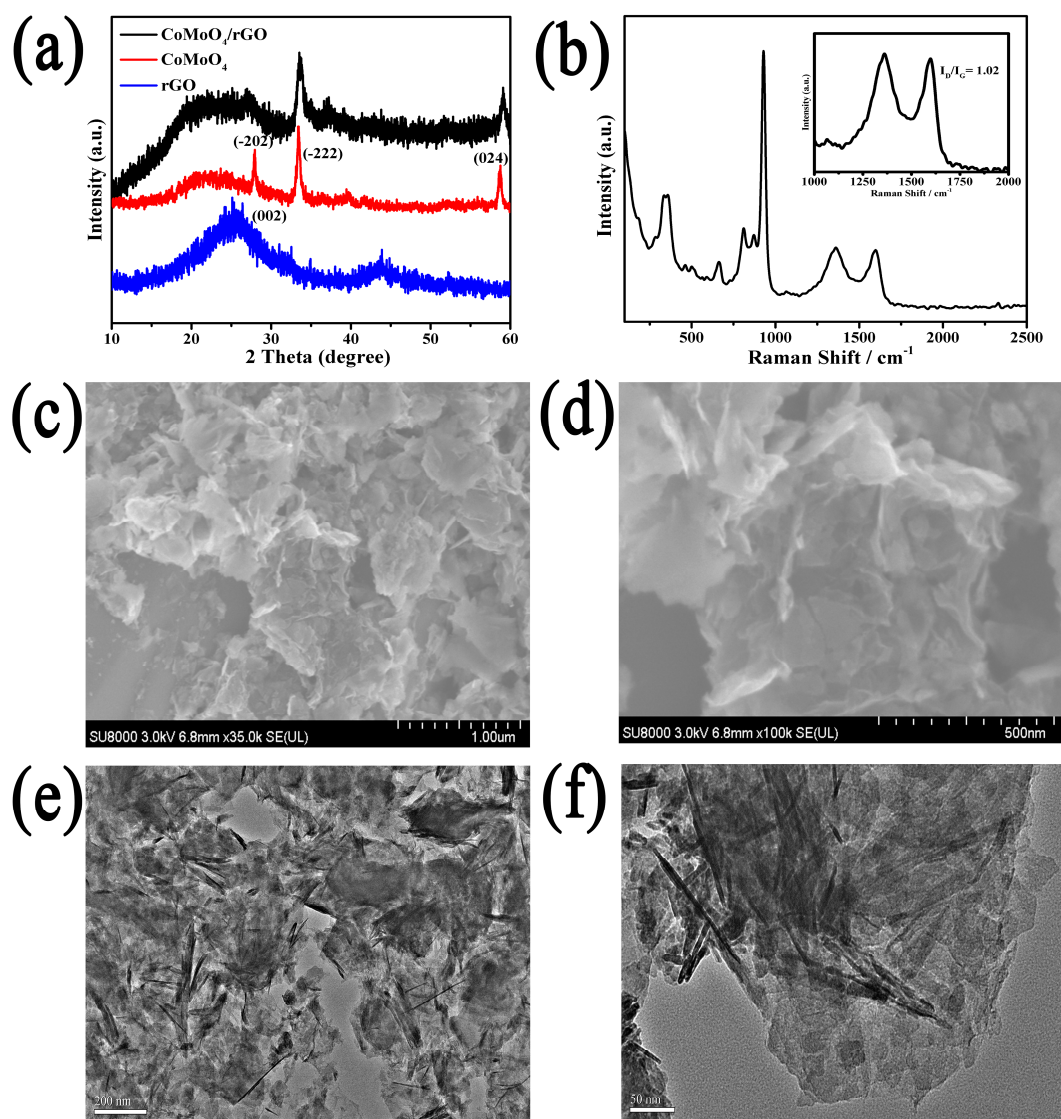

Figure 1. (**a**) X-ray Powder Diffraction (XRD) patterns of $CoMoO_4$/rGO, $CoMoO_4$ and rGO powder samples; (**b**) Raman spectra. GO: graphene oxide. (**c**,**d**) SEM images of $CoMoO_4$/rGO. (**e**,**f**) TEM images of $CoMoO_4$/rGO.

The surface chemical component, element valence of the prepared $CoMoO_4$/rGO composites are evaluated by XPS examination, and the relevant results are shown in Figure 2, which demonstrates that the material mainly contains Co (Figure 2b), Mo (Figure 2c), O (Figure 2d), N (Figure 2e), and C (Figure 2f) elements. Two peaks at 780.9 and 796.9 eV are attributed to Co $2p_{3/2}$ and Co $2p_{1/2}$, separately, implying the existence of Co^{2+} (Figure 2b) which are the active catalytic sites which can promote the ORR [33,34]. Particularly, the splitting doublets of Mo $3d_{3/2}$ and Mo $3d_{5/2}$ peaks at 231.9

and 235.2 eV could be observed in Mo 3d XPS (Figure 2c), and the region width is 3.3 eV (Δ Mo 3d). The region width and the binding energy are characteristics of the Mo^{6+} oxidation state which is consistent with previously published examples [35,36]. In the O 1s spectrum, the peak at 532.7 and 531.1 eV correspond to the C=O and O–C=O bonds (Figure 2d). In the N 1s peak, pyridinic, pyrrolic, graphitic, and oxidized N are noticed in the $CoMoO_4$/rGO (Figure 2e) [37]. The peaks centered at 398.0, 399.3, 400.9, and 403.3 eV correspond to the pyridinic N, pyrrolic N, graphitic N, and oxidized N. The observed peak at 396.7 eV is attributed to the charge transfer from molybdenum to nitrogen [38]. Furthermore, C 1s core level spectrum with 284.7, 286.1, 286.7, 288.4 eV are owing to sp^2 hybridized carbon, sp^2 carbon atoms bonded to nitrogen, C–O groups, and carbonyl carbon (O–C=O) (Figure 2f) [39,40]. The above XPS results affirm that the valence of Co, Mo, and O elements are +2, +6 and −2, respectively. All the above data demonstrate the incorporation of N atoms into the graphene lattice which was due to the treatment with ammonia solution. The types of pyridinic N and graphitic N in graphene have a profound effect on the ORR catalytic performance.
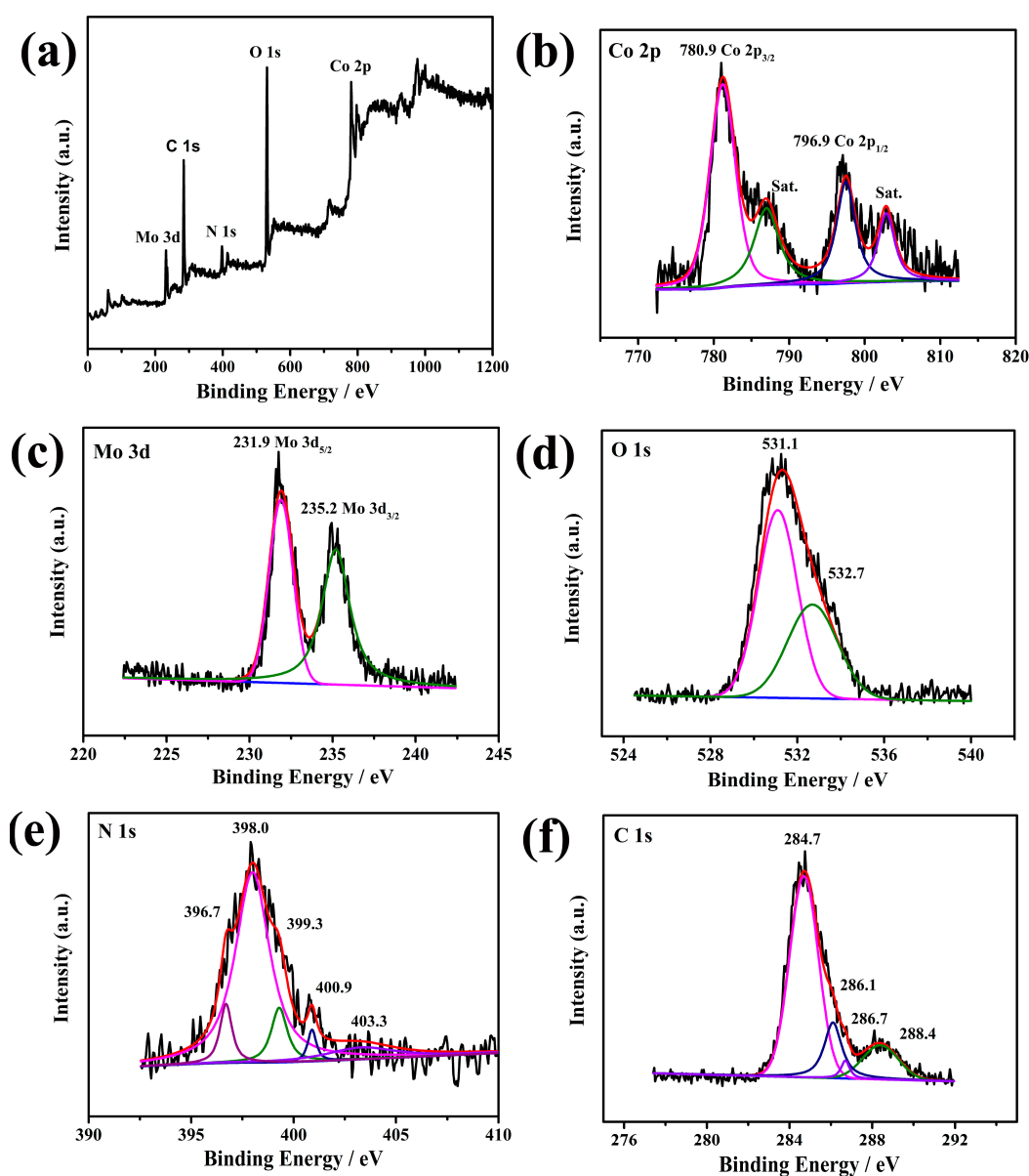

Figure 2. (**a**) the XPS survey of $CoMoO_4$/rGO; (**b**) Co 2p XPS peaks; (**c**) Mo 3d XPS peaks; (**d**) O 1s XPS spectrum; (**e**) N 1s XPS spectrum; (**f**) C 1s peaks XPS.

FT-IR measurements were carried out in an effort to investigate further the structural features of the synthesized composite material, Figure 3 shows the FT-IR spectra of $CoMoO_4/rGO$ powders. The broad peak centered at 3442 cm^{-1} is owing to the hydroxyl (O–H) stretching mode [41] while the one located at 1624 cm^{-1} verified the existence of O–H bending vibrations of water molecule. The spectra of $CoMoO_4/rGO$ sample revealed peaks centereda at 924 and 864 cm^{-1} ascribe to the symmetric and asymmetric stretching vibration of O–Mo–O [42]. However, a peak located at 672 cm^{-1} is ascribed to Co–Mo–O stretching vibration [43].
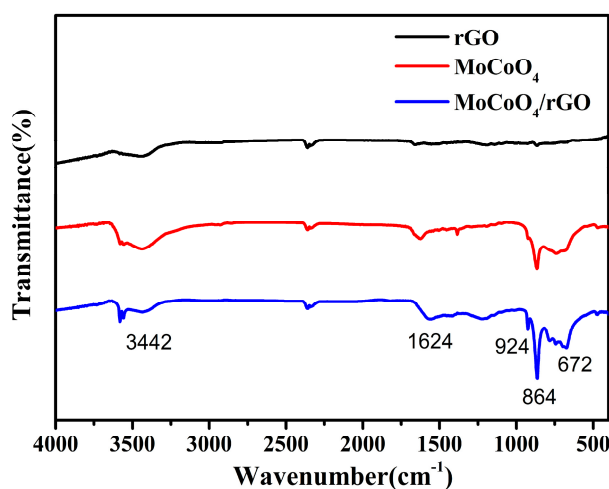

Figure 3. FTIR spectra of the $CoMoO_4$, rGO, and $CoMoO_4/rGO$.

Cyclic voltammetry (CV) is a quite informative technique regarding the investigation of the ORR activity of a nanomaterial. CV was carried out at 25 °C in the presence of N_2 or O_2 under alkaline condition using a standard three-electrode cell. As shown in Figure 4a, the $CoMoO_4/rGO$ catalyst shows a clear cathodic redox peak (0.78 V) in O_2-purged electrolyte but not in N_2-saturated solution. This observation is indicative of the $CoMoO_4/rGO$ composite's catalytic activity toward ORR. LSV studies provided additional proof of the material's activity using a rotating disk electrode (RDE) or rotating ring disk electrode (RRDE). In a similar fashion to the CV experiments, linear sweep voltammetry (LSV) was employed under the same experimental conditions (O_2-saturated electrolyte) with predefined rotation speeds at 25 °C. As soon as the working electrode reached the desired rotation speed, the observed changes of current density were recorded. Figure 4b, $CoMoO_4/rGO$ illustrates the observed onset potential at 0.89 V which is higher than of the one obtained for the pristine $CoMoO_4$. The improved electrochemical activity of the $CoMoO_4/rGO$ composite can be explained as follows; on one hand, the rGO contains pyridinic N and graphitic N, the two types of nitrogen influence the ORR catalytic activity and can improve the overall performance. On the other hand, the $CoMoO_4$ doping of rGO hinders the aggregation of graphene, the $CoMoO_4$ can disperse onto rGO which can expose more cobalt based active sites. The Co^{2+} plays a crucial role in ORR catalytic process [33,34]. Thus, the $CoMoO_4/rGO$ composite exhibits more exposed and accessible active sites compared with the pristine $CoMoO_4$. Among them, commercial Pt/C material exhibits an onset potential at 0.92 V and a limiting current density of ~5.5 mA cm^{-2}. We made an effort to compare the ORR catalytic activity between the $CoMoO_4/rGO$ composite and other catalysts reported previously (Table S1). Figure 4c shows the RDE linear sweep voltammetry analysis for the ORR of the $CoMoO_4/rGO$ electrode at rotation speeds ranging from 100 rpm to 2500 rpm. It can be observed that the limiting density of the $CoMoO_4/rGO$ increases as a function of the rotation speed. The diffusion-limiting current density increases as the rotating speed increases, due to the shortened diffusion distance at high rotation speed.
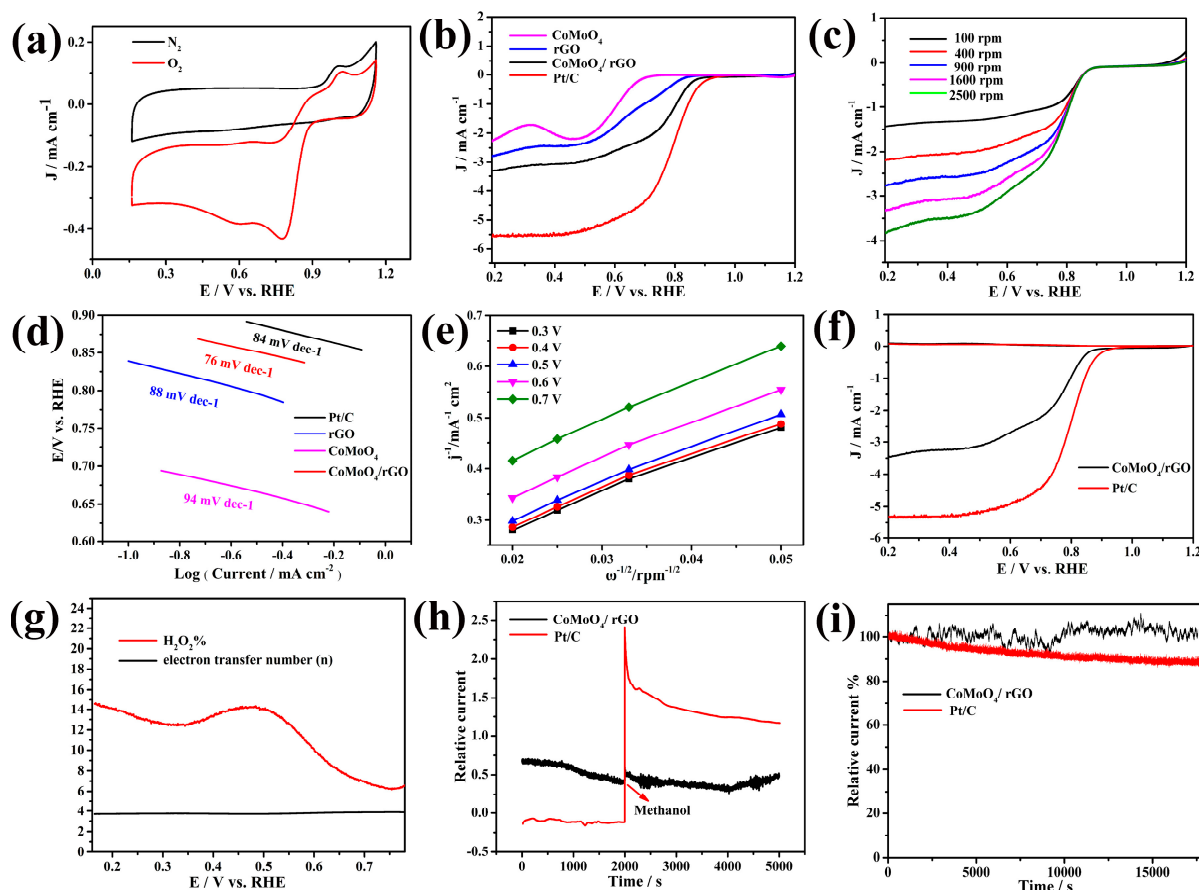
Figure 4. (**a**) CV curves of $CoMoO_4$/rGO in O_2-saturated (red line) or N_2-saturated (black line) 0.1 M KOH with a scan rate of 10 mV s^{-1}; (**b**) linear sweep voltammetry (LSV) curves of $CoMoO_4$, rGO, $CoMoO_4$/rGO, and Pt/C nanocomposites in O_2-saturated 0.1 M KOH with a sweep rate of 5 mV s^{-1} at 1600 rmp; (**c**) LSV curves of $CoMoO_4$/rGO at various rotation speeds with a sweep of 5 mV s^{-1}; (**d**) Tafel plots of $CoMoO_4$, rGO, $CoMoO_4$/rGO, and Pt/C in O_2 saturated 0.1 M KOH at a scan rate of 5 mV/s, rotation rate = 1600 rpm; (**e**) Koutecky–Levich plots of $CoMoO_4$/rGO at different electrode potentials; (**f**) rotating ring disk electrode (RRDE) voltammograms of $CoMoO_4$/rGO and Pt/C; (**g**) The transfer electron number (n) and hydrogen peroxide yield (H_2O_2%) curves of $CoMoO_4$/rGO material; (**h**) Current-time (I-t) curves of $CoMoO_4$/rGO and Pt/C with the addition of 1 M methanol; (**i**) the relative retention of current vs. Time in O_2-saturated 0.1 M KOH solution for $CoMoO_4$/rGO and Pt/C.

LSV studies offer the basis for further understanding of ORR performance. Figure 4b, represent the obtained tafel plots of all catalysts which presented in Figure 4d. The Tafel slope of the rGO, $CoMoO_4$, $CoMoO_4$/rGO, and Pt/C were found to be 88, 94, 76, and 84 mV/dec, respectively. It is worth noting that the rGO and $CoMoO_4$/rGO have a Tafel slope of 88 and 76 mV/dec, respectively, which is quite close to the one observed for Pt/C (84 mV/dec). This means that rGO and $CoMoO_4$/rGO have similar ORR kinetics to the Pt/C. The relevant Kouteckye-Levich (K-L) curves (Figure 4e) at 0.3–0.7 V display good linear relationship. As computed from the slopes of the K-L curves (Figure 4e), the electron-transfer number (n) values are 4.25, 4.23, 4.09, 4.03, and 3.79 at 0.3, 0.4, 0.5, 0.6, and 0.7 V (vs. reversible hydrogen electrode (RHE)), respectively. The number of transferred electrons (n) and the H_2O_2 yield were estimated based on the Equations (S1) and (S2) (see Supplementary Materials). The number of transferred electrons (n) and peroxide yields were calculated from the obtained RRDE (Figure 4f) curves. Form Figure 4g, the n was found to be 3.8–3.9 in a range of potential values of 0.1 to 0.8 V (vs. RHE) for $CoMoO_4$/rGO. This means that the ORR on $CoMoO_4$/rGO follows a 4e$^-$ pathway with a low H_2O_2 (mean value less than 15%) production yield. The number of transferred electrons (n)

of CoMoO$_4$/rGO is the same as the Pt/C, and the result certifies that the ORR own a four-electron mechanism on CoMoO$_4$/rGO. The promising catalytic activity originates from the structural features of CoMoO$_4$/rGO which ensures a high-density of accessible active sites. The methanol tolerance and electrochemical stability are vital for the evaluation of the catalytic activity of ORR electrocatalysts. In Figure 4h, CoMoO$_4$/rGO did not show significant current change after addition of 1 M methanol at 2000 s, where the relative current density of the Pt/C electrode was significantly decreased. The result shows that the CoMoO$_4$/rGO composite has better resistance to methanol. The stability of CoMoO$_4$/rGO was tested further using chronoamperometric measurements in 0.1 M KOH electrolyte. As shown in Figure 4i, the CoMoO$_4$/rGO maintains the initially observed current after 18,000 s. On the contrary, the current density of Pt/C drops to 84%. These data demonstrate that the CoMoO$_4$/rGO composite exhibits better stability than Pt/C.

3. Experimental Section

3.1. Chemicals and Materials

Cobalt(II) chloride hexahydrate (CoCl$_2$·6H$_2$O), ammonium molybdate tetrahydrate ((NH$_4$)$_6$Mo$_7$O$_{24}$·24H$_2$O), urea, ethanol and potassium hypermanganate were acquired from Beijing Chemical Reagent Co. Ltd. (Beijing, China). Nafion (5 wt %) and commercial Pt/C (20 wt %) catalysts were obtained from DuPont (DuPont, Shanghai, China) and Johnson Matthey (Johnson Matthey, Shanghai, China), respectively. Flake graphite was acquired from Qingdao Risheng graphite Ltd. (Qingdao, China). All chemicals were all directly applied without any further purification. Ultrapure water (18.25 MΩ cm^{-2}) was offered by Water Purifier system and used for all aqueous solution.

3.2. Synthesis of Graphene Oxide (GO)

Graphene oxide was prepared with the improved method reported in the literature [44]. For the improved method, the mixed acid of 360 mL H$_2$SO$_4$ and 40 mL H$_3$PO$_4$ was slowly added to a large drying beaker containing 3 g graphite flakes and 18 g KMnO$_4$ mixed solid, the exothermic reaction led to the increase of the temperature of the reaction system. Then the resultant solution was kept at 50 °C and oscillated for 12 h. After cooling to ambient temperature, about 400 mL of ice water and 3 mL 30% H$_2$O$_2$ slowly poured into the reaction under vigorous stirring, changing the color of the resultant from dark brown to bright yellow. The prepared product was rinsed several times with H$_2$O and filtered. The as-synthesized sample was dried at room temperature.

3.3. Synthesis of CoMoO$_4$/rGO Catalysts

0.1185 g CoCl$_2$·6H$_2$O (0.5 mmol), 0.877 g (NH$_4$)$_6$Mo$_7$O$_{24}$·24H$_2$O (0.5 mmol) were dissolved in 10 mL of deionized water (DI) and stirred for 10 min to form CoMoO$_4$ solution. Then 72.6 mg GO (ρ = 6.6 g/L) dispersion was added into the CoMoO$_4$ solution. Meanwhile, 29 mL distilled water was poured into the reaction mixture. The mixture was agitated for 1 h and formed a clear solution. After 1 h, the pH of the solution was adjusted to 10 using ammonia solution (25~28%). The homogenous solution was placed into an autoclave. The autoclave was sealed and maintained at 120 °C for 12 h. After cooling down to ambient temperature, the product was filtered, rinsed several times with distilled water and dried at 60 °C overnight. For comparison, rGO and CoMoO$_4$ samples were also prepared in a similar manner in the absence of CoMoO$_4$ or GO, respectively.

4. Conclusions

Graphene-supported, cross-linked CoMoO$_4$/rGO nanosheets were fabricated employing a facile one-pot hydrothermal approach. The CoMoO$_4$/rGO hybrid material revealed an improved catalytic performance for the oxygen reduction reaction, comparing to the pristine CoMoO$_4$ and rGO. Furthermore, CoMoO$_4$/rGO displays a remarkable durability towards the ORR compared to the Pt/C

in alkaline medium. The electrocatalytic activity of the as-synthesized $CoMoO_4$/rGO can be attributed to: (1) the molybdenum based induced fast electron transfer processes; (2) the $CoMoO_4$ doping of rGO hinders the aggregation of graphene leading to uniform dispersion of $CoMoO_4$ onto rGO; and (3) the overall synergistic effect between $CoMoO_4$ and rGO improved the accessibility of more cobalt based active sites. The observed improvement of the electrochemical properties renders the $CoMoO_4$/rGO composite material as a highly promising electrode material for energy related applications such as manufacturing of cost-affordable fuel cells.

Supplementary Materials: The following are available online at www.mdpi.com/2073-4344/7/12/375/s1, Figure S1. Raman spectra of graphene oxide, Table S1. Comparison of ORR activity parameters with other recently reported. 1. Physical characterization, 2. Electrochemical measurements.

Author Contributions: Jiaqi Fu and Jiang-Li Meng have contributed equally. Jiaqi Fu wrote the paper, Jiaqi Fu and Jiang-Li Meng did the experiments. Mei-Jie Wei contributed analysis tools and reagents. Hong-Ying Zang and Haralampos N. Miras revised the article. Hong-Ying Zang, Hua-Qiao Tan, Yong-Hui Wang, Yang-Guang Li, Jiaqi Fu, Jiang-Li Meng, and Mei-Jie Wei analyzed the data.

Conflicts of Interest: The authors declare no conflict of interest.

References

1. Canadell, J.G.; Quéré, C.L.; Raupach, M.R.; Field, C.B.; Buitenhuis, E.T.; Ciais, P.; Conway, T.J.; Gillett, N.P.; Houghton, R.A.; Marland, G. Contributions to accelerating atmospheric CO_2 growth from economic activity, carbon intensity, and efficiency of natural sinks. *Proc. Natl. Acad. Sci. USA* **2007**, *104*, 18866–18870. [CrossRef] [PubMed]

2. Hoel, M.; Kverndokk, S. Depletion of fossil fuels and the impacts of global warming. *Resour. Energy Econ.* **1996**, *18*, 115–136. [CrossRef]

3. Shafiee, S.; Topal, E. When will fossil fuel reserves be diminished? *Energy Policy* **2009**, *37*, 181–189. [CrossRef]

4. Du, Z.; Li, H.; Gu, T. A state of the art review on microbial fuel cells: A promising technology for wastewater treatment and bioenergy. *Biotechnol. Adv.* **2007**, *25*, 464–482. [CrossRef] [PubMed]

5. Watanabe, M.; Tryk, D.A.; Wakisaka, M.; Yano, H.; Uchida, H. Overview of recent developments in oxygen reduction electrocatalysis. *Electrochim. Acta* **2012**, *84*, 187–201. [CrossRef]

6. Steele, B.C.H.; Heinzel, A. Materials for fuel-cell technologies. *Nature* **2001**, *414*, 345–352. [CrossRef] [PubMed]

7. Debe, M.K. Electrocatalyst approaches and challenges for automotive fuel cells. *Nature* **2012**, *486*, 43–51. [CrossRef] [PubMed]

8. Cao, R.; Thapa, R.; Kim, H.; Xu, X.; Kim, M.G.; Li, Q.; Park, N.; Liu, M.; Cho, J. Promotion of oxygen reduction by a bio-inspired tethered iron phthalocyanine carbon nanotube-based catalyst. *Nat. Commun.* **2013**, *4*, 2076. [CrossRef] [PubMed]

9. Li, Y.; Gong, M.; Liang, Y.; Feng, J.; Kim, J.E.; Wang, H.; Hong, G.; Zhang, B.; Dai, H. Advanced zinc-air batteries based on high-performance hybrid electrocatalysts. *Nat. Commun.* **2013**, *4*, 1805. [CrossRef] [PubMed]

10. Wu, T.; Zhang, L. Metal molybdate nanorods as non-precious electrocatalysts for the oxygen reduction. *Funct. Mater. Lett.* **2015**, *8*, 3. [CrossRef]

11. Stamenkovic, V.R.; Fowler, B.; Mun, B.S.; Wang, G.; Ross, P.N.; Lucas, C.A.; Markovic, N.M. Improved oxygen reduction activity on $Pt_3Ni(111)$ via increased surface site availability. *Science* **2007**, *315*, 493–497. [CrossRef] [PubMed]

12. Winter, M.; Brodd, R.J. What are batteries, fuel cells, and supercapacitors? *Chem. Rev.* **2004**, *104*, 4245–4270. [CrossRef] [PubMed]

13. Xiao, W.; Wang, D.; Lou, X. Shape-Controlled Synthesis of MnO_2 Nanostructures with Enhanced Electrocatalytic Activity for Oxygen Reduction. *J. Phys. Chem. C* **2009**, *114*, 1694–1700. [CrossRef]

14. Xu, Y.; Jiang, H.; Li, X.; Xiao, H.; Xiao, W.; Wu, T. Synthesis and characterization of Mn-based composite oxides with enhanced electrocatalytic activity for oxygen reduction. *J. Mater. Chem. A* **2014**, *2*, 13345. [CrossRef]

15. Lu, Q.; Zhou, Y. Hierarchical polythiophene-coated MnO$_2$ nanosheets as non-precious electro-catalyst to oxygen reduction. *Funct. Mater. Lett.* **2010**, *3*, 89–92. [CrossRef]

16. Liang, Y.; Li, Y.; Wang, H.; Zhou, J.; Wang, J.; Regier, T.; Dai, H. Co$_3$O$_4$ nanocrystals on graphene as a synergistic catalyst for oxygen reduction reaction. *Nat. Mater.* **2011**, *10*, 780–786. [CrossRef] [PubMed]

17. Vezzù, K.; Delpeuch, A.B.; Negro, E.; Polizzi, S.; Nawn, G.; Bertasi, F.; Pagot, G.; Artyushkova, K.; Atanassov, P.; Noto, V.D. Fe-carbon nitride "Core-shell" electrocatalysts for the oxygen reduction reaction. *Electrochim. Acta* **2016**, *222*, 1778–1791. [CrossRef]

18. Gokhal, R.; Chen, Y.; Serov, A.; Artyushkova, K.; Atanassov, P. Novel dual templating approach for preparation of highly active Fe-N-C electrocatalyst for oxygen reduction. *Electrochim. Acta* **2017**, *224*, 49–55. [CrossRef]

19. Karthikeyan, K.; Kalpana, D.; Renganathan, N.G. Synthesis and characterization of ZnCo$_2$O$_4$ nanomaterial for symmetric supercapacitor applications. *Ionics* **2009**, *15*, 107–110. [CrossRef]

20. Bao, L.; Zang, J.; Li, X. Flexible Zn$_2$SnO$_4$/MnO$_2$ Core/Shell Nanocable-Carbon Microfiber Hybrid Composites for High-Performance Supercapacitor Electrodes. *Nano Lett.* **2011**, *11*, 1215–1220. [CrossRef] [PubMed]

21. Shen, L.; Che, Q.; Li, H.; Zhang, X. Mesoporous NiCo$_2$O$_4$ Nanowire Arrays Grown on Caibon Textiles as Binder- Free Flexible Electrodes for Energy Storage. Adv. *Funct. Mater.* **2014**, *24*, 2630–2637. [CrossRef]

22. Cai, D.; Liu, B.; Wang, D.; Liu, Y.; Wang, L.; Li, H.; Wang, Y.; Wang, C.; Li, Q.; Wang, T. Facile hydrothermal synthesis of hierarchical ultrathin mesoporous NiMoO$_4$ nanosheets for high performance supercapacitors. *Electrochim. Acta* **2014**, *115*, 358–363. [CrossRef]

23. Cai, D.; Liu, B.; Wang, D.; Wang, L.; Liu, Y.; Li, H.; Wang, Y.; Li, Q.; Wang, T. Construction of unique NiCo$_2$O$_4$ nanowire@CoMoO$_4$ nanoplate core/shell arrays on Ni foam for high areal capacitance supercapacitors. *J. Mater. Chem. A* **2014**, *2*, 4954–4960. [CrossRef]

24. Yu, X.; Lu, B.; Xu, Z. Super Long-Life Supercapacitors Based on the Construction of Nanohoneycomb-Like Strongly Coupled CoMoO$_4$–3D Graphene Hybrid Electrodes. *Adv. Mater.* **2014**, *26*, 1044–1051. [CrossRef] [PubMed]

25. Osgood, T.; Devaguptapu, S.V.; Xu, H.; Cho, J.; Wu, G. Transition metal (Fe, Co, Ni, and Mn) oxides for oxygen reduction and evolution bifunctional catalysts in alkaline media. *Nano Today* **2016**, *11*, 601–625. [CrossRef]

26. Li, M.; Xu, S.; Cherry, C.; Zhu, Y.; Wu, D.; Zhang, C.; Zhang, X.; Huang, R.; Qi, R.; Wang, L.; Chu, P.K. Hierarchical 3-dimensional CoMoO$_4$ nanoflakes on a macroporous electrically conductive network with superior electrochemical performance. *J. Mater. Chem. A* **2015**, *3*, 13776–13785. [CrossRef]

27. Cheng, F.; Shen, J.; Peng, B.; Pan, Y.; Tao, Z.; Chen, J. Rapid room-temperature synthesis of nanocrystalline spinels as oxygen reduction and evolution electrocatalysts. *Nat. Chem.* **2011**, *3*, 79–84. [CrossRef] [PubMed]

28. Mu, Y.; Liang, H.; Hu, J.; Jiang, L.; Wan, L. Controllable Pt Nanoparticle Deposition on Carbon Nanotubes as an Anode Catalyst for Direct Methanol Fuel Cells. *J. Phys. Chem. B* **2005**, *109*, 22212–22216. [CrossRef] [PubMed]

29. Liang, Y.; Li, Y.; Wang, H.; Dai, H. Strongly Coupled Inorganic/Nanocarbon Hybrid Materials for Advanced Electrocatalysis. *J. Am. Chem. Soc.* **2013**, *135*, 2013–2036. [CrossRef] [PubMed]

30. Liang, Y.; Wang, H.; Zhou, J.; Li, Y.; Wang, J.; Regier, T.; Dai, H. Covalent Hybrid of Spinel Manganese-Cobalt Oxide and Graphene as Advanced Oxygen Reduction Electrocatalysts. *J. Am. Chem. Soc.* **2012**, *134*, 3517–3523. [CrossRef] [PubMed]

31. Sun, M.; Liu, H.; Liu, Y.; Qu, J.; Li, J. Graphene-based transition metal oxide nanocomposites for the oxygen reduction reaction. *Nanoscale* **2015**, *7*, 1250–1269. [CrossRef] [PubMed]

32. Dou, S.; Shen, A.; Tao, L.; Wang, S. Molecular doping of graphene as metal–free electrocatalyst for oxygen reduction reaction. *Chem. Commun.* **2014**, *50*, 10672–10675. [CrossRef] [PubMed]

33. Zhuang, L.; Ge, L.; Yang, Y.; Li, M.; Jia, Y.; Yao, X.; Zhu, Z. Ultrathin Iron-Cobalt Oxide Nanosheets with Abundant Oxygen Vacancies for the Oxygen Evolution Reaction. *Adv. Mater.* **2017**, *29*, 1606793. [CrossRef] [PubMed]

34. Song, W.; Ren, Z.; Chen, S.; Meng, Y.; Biswas, S.; Nandi, P.; Elsen, H.A.; Gao, P.; Suib, S.L. Ni- and Mn-Promoted Mesoporous Co_3O_4: A Stable Bifunctional Catalyst with Surface-Structure-Dependent Activity for Oxygen Reduction Reaction and Oxygen Evolution Reaction. *ACS Appl. Mater. Interfaces* **2016**, *8*, 20802–20813. [CrossRef] [PubMed]

35. Yu, M.; Jiang, L.; Yang, H. Ultrathin nanosheets constructed $CoMoO_4$ porous flowers with high activity for electrocatalytic oxygen evolution. *Chem. Commun.* **2015**, *51*, 14361–14364. [CrossRef] [PubMed]

36. Wang, B.; Li, S.; Wu, X.; Liu, J.; Tian, W.; Chen, J. Self-assembly of ultrathin mesoporous $CoMoO_4$ nanosheet networks on flexible carbon fabric as a binder-free anode for lithium-ion batteries. *New J. Chem.* **2016**, *40*, 2259–2267. [CrossRef]

37. Zhang, C.; Hao, R.; Liao, H.; Hou, Y. Synthesis of amino-functionalized graphene as metal–free catalyst and exploration of the roles of various nitrogen states in oxygen reduction reaction. *Nano Energy* **2013**, *2*, 88–97. [CrossRef]

38. Baraldi, A.; Brena, B.; Cocco, D.; Comelli, G.; Lizzit, S.; Paolucci, G.; Baumann, P.; Scheuch, V.; Uebing, C. The structure of the MoN surface compound on Fe-3.5%Mo-N (100) studied by X-ray photoelectron diffraction: First results from ELElTRA. *Vacuum* **1997**, *48*, 351–355. [CrossRef]

39. Gao, S.; Geng, K.; Liu, H.; Wei, X.; Zhang, M.; Wang, P.; Wang, J. Transforming organic-rich amaranthus waste into nitrogen-doped carbon with superior performance of the oxygen reduction reaction. *Energy Environ. Sci.* **2015**, *8*, 221–229. [CrossRef]

40. Liu, Z.; Zhao, Z.; Wang, Y.; Dou, S.; Yan, D.; Liu, D.; Xia, Z.; Wang, S. In Situ Exfoliated, Edge-Rich, Oxygen-Functionalized Graphene from Carbon Fibers for Oxygen Electrocatalysis. *Adv. Mater.* **2017**, *29*, 1606207. [CrossRef] [PubMed]

41. Tsay, J.D.; Fang, T.T. Effects of Molar Ratio of Citric Acid to Cations and of pH Value on the Formation and Thermal-Decomposition Behavior of Barium Titanium Citrate. *J. Am. Ceram. Soc.* **1999**, *82*, 1409–1415. [CrossRef]

42. Moura, A.P.D.; Oliveira, L.H.D.; Pereira, P.F.S.; Rosa, I.L.V.; Li, M.S.; Longo, E.; Varela, J.A. Photoluminescent Properties of $CoMoO_4$ Nanorods Quickly Synthesized and Annealed in a Domestic Microwave Oven. *Adv. Chem. Eng. Sci.* **2012**, *2*, 465–473. [CrossRef]

43. Sieber, K.; Kershaw, R.; Dwight, K.; Wold, A. Dependence of Magnetic Properties on Structure in the Systems $NiMoO_4$ and $CoMoO_4$. *Inorg. Chem.* **1983**, *22*, 2667–2669. [CrossRef]

44. Marcano, D.C.; Kosynkin, D.V.; Berlin, J.M.; Sinitskill, A.; Sun, Z.; Slesarev, A.; Alemany, L.B.; Lu, W.; Tour, J.M. Improved synthesis of graphene oxide. *ACS Nano* **2010**, *4*, 4806–4814. [CrossRef] [PubMed]